Journal of Materials Chemistry C

ROYAL SOCIETY OF CHEMISTRY

PAPER

View Article Online
View Journal | View Issue

Open Access Article. Published on 25 May 2024. Downloaded on 3/17/2026 1:04:52 PM.
This article is licensed under a Creative Commons Attribution 3.0 Unported Licence.

Check for updates

Cite this: J. Mater. Chem. C, 2024, 12, 8705

Six metal cations in one double perovskite: exploring complexity of chloride elpasolites by high-throughput experimentation†

Oleksandr Stroyuk,*[a] Oleksandra Raievska,[b] Manuel Daum,[ab] Jens Hauch[ab] and Christoph J. Brabec[ab]

Received 25th April 2024,
Accepted 24th May 2024

DOI: 10.1039/d4tc01693a

rsc.li/materials-c

A high-throughput screening of lead-free double chloride perovskites $Cs_2M^IM^{III}Cl_6$ is performed combining combinatorial robot-assisted synthesis with accelerated structural and spectral characterizations. The screening encompasses about 350 elpasolite compounds with broad variations of the M^{III} site, including combinations of two (Bi + In, Bi + Sb, and In + Sb) and three cations (In + Bi + Sb and Fe + Bi + In). The robot-assisted open-environment synthesis protocol allows the double perovskites with these M^{III} combinations and Ag^+/Na^+-occupied M^I site to be produced using a general routine in the form of single-phase microcrystalline solid solutions with reliably controlled composition. The high-throughput screening revealed a series of non-additive effects arising from the combination of multiple cations on the M^{III} site, including a "volcano"-shaped dependence of the photoluminescence quantum yield of $Cs_2(Ag,Na)(Bi,In)Cl_6$ elpasolites on Ag/Na and Bi/In ratio and band-bowing effects in the compositional dependences of the bandgaps of perovskites with Bi + Sb, In + Bi + Sb, and Fe + Bi + In combinations. In the latter case, the accelerated screening resulted in the double chloride perovskites with an unusually low indirect bandgap of 1.64 eV.

1 Introduction

The uprise of studies of lead-based halide perovskites as highly promising light-sensitive, light-harvesting, and light-emitting materials[1–5] fueled interest in lead-free structural analogs, which can potentially show similar unique photophysical and charge transport properties, while being more photochemically stable and environmentally benign.[6–10] Like their lead-based counterparts, many lead-free halide perovskites showed remarkable functional properties that can be harvested in LED technologies, X-ray detectors and photodetectors, photovoltaics (PV), photocatalysis, and other emerging applications.[6–17]

As a remarkable class of lead-free perovskites, the double halide (elpasolite) perovskites $A^I{}_2M^IM^{III}X_6$, where A^I is an alkali metal (organic) cation, M^I and M^{III} are the "main" lead-substituting metal components, and X is a halide, reveal an unprecedented variability of their structure, allowing the composition of all four sites, A, M^I, M^{III}, and X, to be varied independently.[6,7,10,11,18] By considering only single occupants for each of the crystallographic sites, the potential compositional variability of elpasolites is already expected to be impressive, with A^I = Cs or Rb, M^I = Ag, Na or K, M^{III} = Bi, In, Sb, Au, Fe, lanthanides, *etc.*, and X = Cl, Br, I. This variability is further increased by orders of magnitude due to the unique structural tolerance of double perovskites allowing two or more cations to be alloyed on each of the metal positions, as well as two to three halide species to be combined in different proportions on the X site.[7,8,10,11,14,18]

The studies of double halide perovskites with multiple M^I and M^{III} components are driven by a large potential for non-additive effects arising from the homogeneous mixing of several metal cations with similar sizes. One of the most prominent examples of such non-additive effects is the family of $Cs_2Ag_xNa_{1-x}Bi_yIn_{1-y}Cl_6$ solid-solution compounds (abbreviated as CANBIC by the first letters of constituent elements).[10,19–22] In this family, a partial substitution of sodium with silver (or *vice versa*) in In-pure or Bi-pure perovskites changes the lattice symmetry and selection rules of the photophysical processes, resulting in the radiative recombination from the self-trapped exciton (STE) states and emission of bright and broadband photoluminescence (PL).[19,20] Further introduction of bismuth on M^{III} sites of In-pure CANIC compounds (or indium – into Bi-pure CANBC compounds) allows the PL quantum yields (QYs) to be boosted

[a] Forschungszentrum Jülich GmbH, Helmholtz-Institut Erlangen Nürnberg für Erneuerbare Energien (HI ERN), 91058 Erlangen, Germany. E-mail: o.stroyuk@fz-juelich.de
[b] Friedrich-Alexander-Universität Erlangen-Nürnberg, Materials for Electronics and Energy Technology (i-MEET), Martensstrasse 7, 91058 Erlangen, Germany

† Electronic supplementary information (ESI) available. See DOI: https://doi.org/10.1039/d4tc01693a

Open Access Article. Published on 25 May 2024. Downloaded on 3/17/2026 1:04:52 PM.
This article is licensed under a Creative Commons Attribution 3.0 Unported Licence.

to almost 100%.[10,23–25] Another remarkable example of the non-additivity upon the homogeneous M^{III} alloying in elpasolites is the band-bowing effect in $Cs_2AgBi_xSb_{1-x}Cl_6$ perovskites, where the Bi/Sb alloying results in the compounds with lower bandgaps as compared to Bi- and Sb-pure perovskites.[26]

The tolerance of elpasolites to multiple homogeneous alloying on all four crystallographic positions as well as to the introduction of various homo- and heterovalent dopants[7,10,18] can result in hundreds of thousands of possible compounds even for the limited element list discussed above. In this situation, searching for non-additivity effects requires an upscaling from the experiments targeting specific compounds to high-throughput (HTP) experimentation. The latter allows hundreds and thousands of perovskite compounds to be screened providing an acceleration factor of ×10 to ×100 as compared to the conventionally reported intuition-driven synthetic approaches. To make accelerated screening possible, unified protocols for the accelerated synthesis of double perovskites of diverse composition need to be developed and combined with the accelerated characterization of structural, spectral, photophysical, and other properties, both orchestrated to provide the same throughput level.

Robot-assisted HTP approaches have already been successfully applied for the accelerated research and discovery of lead-based perovskite materials for PV applications, covering various aspects such as HTP discovery of new cations for A^I and their combinations,[27–33] HTP studies of the formation of perovskite films and their PV activity,[33–38] as well as HTP evaluation of degradation stability of the lead perovskites.[37,39,40]

At the same time, examples of the experimental HTP screening of the lead-free halide perovskite are rather scarce,[41] despite the much higher compositional complexity one can potentially achieve with these compounds. Most reports focus on computational screening of the lead-free halide perovskites by HTP density functional theory calculations, machine learning, and thermodynamic stability evaluation.[42–48] These explorations allowed several databanks on the calculated stability factors and spectral properties of lead-free perovskite compounds to be formed,[43,49–53] still to be complemented by a massive experimental HTP screening of such compounds.

The lack of experimental HTP studies on lead-free perovskites can, at least in part, be related to the challenge of adapting the existing synthesis routines to the regime of accelerated experimentation. Typically, the synthesis of microcrystalline elpasolites includes aggressive agents (concentrated acids for chlorides, volatile, non-stable, or irritating halide sources for bromides and iodides) as well as considerable thermal inputs, such as annealings or supercritical treatments,[6–8,10,11] which can hardly be upscaled or adapted for the robot-assisted procedures necessary to reach the desired acceleration factors. The colloidal syntheses of double perovskite nanocrystals are performed by hot injection/heating-up protocols at elevated temperatures in coordinating solvents,[6,17] also posing restrictions for upscaling and automation.

To address this challenge, we focused on the development of simpler and milder protocols for the synthesis of double halide perovskites, which can be performed in an open environment at room temperature (RT), avoiding thermal treatments and aggressive components, and can be easily adapted for the robot-assisted HTP experimentation and upscaled in terms of the composition and yield of the products. The first examples of such "green" synthesis were reported by our group for several chloride elpasolite families, including CANBIC,[23–25] $Cs_2Ag_xNa_{1-x}Fe_yIn_{1-y}Cl_6$,[54] and $Cs_2AgBi_xSb_{1-x}Cl_6$ (CABSC) perovskites.[26] These protocols are based on equalizing the reactivity of different cations in precursors (for example, binding Ag^+ and Bi^{3+} in complexes with ammonia and chloride, respectively) to avoid side hydrolytic reactions and yield highly crystalline perovskite products at RT. The metal reactivity equalization allows different combinations of metals (Bi + In, Bi + Sb, Fe + In, *etc.*) to be introduced on the M^{III} site with minimal adjustments to the synthesis routine. The syntheses were optimized to result exclusively in single-phase perovskites and provide reliable control over the composition of the products, in particular, over the metal ratios on the M^{III} site. At that, the post-synthesis treatments are reduced to a minimum, requiring only a precipitation/re-dispersion-based purification. As an exemplary case, the CABSC perovskites were further converted into bromide or iodide compounds by relatively simple anion-exchange procedures using green halide sources (NaBr and NaI),[26] showing the feasibility of the proposed approach for the synthesis of the whole domain of possible $A^IM^IM^{III}X_6$ compositions.

The present paper is based on our earlier reports, further extending the open-environment green synthesis approach to the larger scale of HTP experimentation. Focusing on chloride elpasolites, we develop a robot-assisted synthesis of multiple sets of double perovskites with variable M^I (Ag + Na) and M^{III} sites, the latter combining two (Bi + In, Bi + Sb, In + Sb) and even three (In + Bi + Sb, Fe + Bi + In) metal cations. The HTP synthesis is accompanied by the HTP characterization showing non-additive spectral effects for $Cs_2(Ag,Na)(Bi,In)Cl_6$, $Cs_2(Ag,Na)(Bi,Sb)Cl_6$, $Cs_2(Ag,Na)(In,Bi,Sb)Cl_6$, and $Cs_2(Ag,Na)(Fe,Bi,In)Cl_6$ families of elpasolites.

2 Results and discussion

2.1 General workflow and description of sample arrays

Recently we have reported an open-atmosphere synthesis of CANBIC elpasolites allowing both Ag/Na and Bi/In ratios to be independently and controllably varied while producing single-phase cubic perovskite products in the entire range of possible compositions.[23–25] The clue to synthesizing single-phase products is in separating metal cations into two precursors, M^{III} = Bi + In in precursor #1 and M^I = Cs + Ag + Na in precursor #2. At that, side hydrolysis reactions in precursor #1 need to be suppressed by adding moderately concentrated HCl, while silver ions in precursor #2 should be bound into a complex with ammonia to prevent Ag^+ hydrolysis in a moderately alkaline medium generated by Cs and Na acetates. The mixing of two precursors results in the instant precipitation of

 This journal is © The Royal Society of Chemistry 2024

Open Access Article. Published on 25 May 2024. Downloaded on 3/17/2026 1:04:52 PM.
This article is licensed under a Creative Commons Attribution 3.0 Unported Licence.

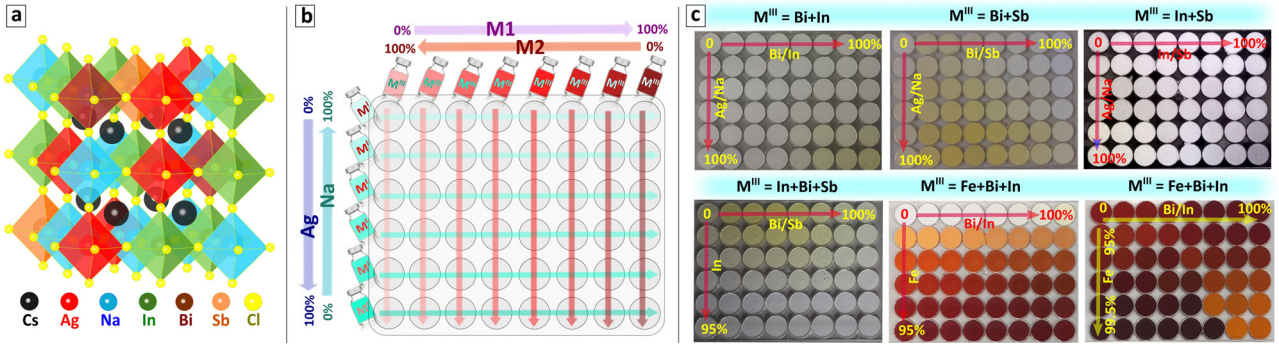

Fig. 1 (a) Schematic structure of double perovskite with In, Bi, and Sb mixed on M^{III} site; (b) scheme of the combinatorial mixing of the M^{I} and M^{III} precursors for the synthesis of binary (M^{III} = M1 + M2) plates; (c) overview of $Cs_2(Ag,Na)M^{III}Cl_6$ double perovskite samples.

single-phase microcrystalline CANBICs at RT requiring no additional thermal treatments.[23,24]

In the present report, we make two steps forward in this synthetic approach. The first step is to adapt the above protocol for automated synthesis using a pipetting robot. The second step is to generalize the automated synthesis and progress from the "pilot" case of M^{III} = Bi + In to other possible combinations, in particular, Bi + Sb and In + Sb, as well as to ternary combinations, such as M^{III} = In + Bi + Sb and Fe + Bi + In. All these compounds are single-phase perovskite solid solutions, indicating a random distribution of up to five types of octahedra formed by different 6-fold coordinated metal cations, as illustrated in Fig. 1(a) for M^{I} = Ag + Na and M^{III} = In + Bi + Sb.

Upscaling of perovskite synthesis to automated HTP regime. The manual open-atmosphere synthesis of double chloride perovskites was upscaled to an HTP regime using an automated platform based on a Tecan pipetting robot, similar to that earlier reported by our group.[28,40] Detailed descriptions of all experimental procedures and characterizations are presented in ESI.†

The main synthesis stage consists of a four-channel pipetting robot with programmable movements in XYZ directions combined with auxiliary elements, such as tip and precursor storage stations, heating, and shaking stations, automated plate-reading spectrometer, and others (ESI,† Fig. S1). The synthesis is controlled from a PC by a dedicated script and recorded by an array of video cameras.

To enable using a single general script for all syntheses we unified the synthesis protocol by increasing the number of manually prepared precursors from 2 to 14.

For the particular cases of binary M^{III} mixtures (M^{III} = M1 + M2 = Bi + In, Bi + Sb, or In + Sb), eight M^{III} precursors with a varied M1/M2 ratio and six M^{I} precursors with a varied Ag/Na ratio were prepared. A combinatorial mixing of eight M^{III} precursors with six M^{I} precursors was then performed on the shaking station by the pipetting robot in an Eppendorf 8 × 6 array microplate with 2.0 mL pit volume resulting in 48 samples. In this way, the x = Ag/(Ag + Na) and y = M1/(M1 + M2) fractions are varied along the shorter and longer axis of the Eppendorf microplate, respectively (see schematic in Fig. 1(b)).

As the first step, a "master" plate of samples with binary M^{III} combinations was always produced with x and y ratios varied from 0 to 1.0. Then, any section of the master plate can be "resolved" into a separate plate with a selected range of x and y simply by changing the precursor concentration and using the same robot-assisted protocol and control script. As an example of such a "focus" plate, a CANBIC sample array is discussed in the present paper with Bi fraction maintained within the range of 0–2% and silver fraction varied from 0 to 100%. By repeating this procedure with different variations of 8 × 6 precursor arrays any desirable number of "focus" plates can be produced by the robotic setup using the same synthetic HTP routine.

For the cases of ternary M^{III} mixtures (M^{III} = M3 + M2 + M1 = In + Bi + Sb or Fe + Bi + In), ten precursor solutions were typically prepared, including eight precursors with a varied M1/M2 ratio as described above for the binary M^{III} cases, as well as an M3 precursor and an M^{I} precursor with a constant nominal Ag/(Ag + Na) fraction. A dedicated control script was developed for ternary M^{III} cases which instructs the pipetting robot to place the same volumes of different M1 + M2 precursors into eight consecutive pits of an Eppendorf 8 × 6 array plate and decrease the M2 + M3 precursor volume for each next row. Then, a similar procedure is performed with the M3 precursor, placing the same volume into eight consecutive wells and increasing the M3 precursor dosage for each next row. After completion, this procedure yields an 8 × 6 array of solutions with the same volume and different M^{III} combinations. At the final step, the robot adds a fixed amount of the M^{I} precursor to each of the 48 wells with M^{III} solutions placed on the shaking station resulting in the precipitation of final perovskite products.

Again, the "master" plates were produced first for all tested M^{III} combinations with the M1/(M1 + M2) and M3/(M1 + M2) fractions changing from 0 to 1.0 along the X and Y axes, respectively, while the nominal Ag/(Ag + Na) fraction is maintained constant. We note, that in a particular case of M^{III} = Fe + Bi + In a higher concentration of HCl was required to maintain the stability of precursors, and for this reason, the synthesis of the Fe-based sample arrays was performed manually under a fume hood.

"Focus" ternary plates can then be produced for any desired compositional domain by adjusting the concentrations of M1 + M2, M3, and Ag/Na precursors and using the same automated HTP (or manual for Fe-based plates) protocol. By applying the

Open Access Article. Published on 25 May 2024. Downloaded on 3/17/2026 1:04:52 PM. This article is licensed under a Creative Commons Attribution 3.0 Unported Licence.

above-discussed protocol a broad number of binary and ternary M^{III} combinations was tested by an automated platform and the sample arrays showing all (or a major part) of samples as single-phase perovskite solid solutions were then selected for the present discussion. Fig. 1(c) provides an overview of the selected sample plates. Considering the complex composition of the perovskite samples we suggest a unified nomenclature of synthesized compounds summarized in Table 1.

As discussed in our previous reports,[23,24] an excess of cesium and sodium salts is typically introduced during the synthesis to shift the ionic equilibria to the formation of Cs-richer double $Cs_2(Ag,Na)M^{III}Cl_6$ perovskite phases ($Cs:M^{III}$ = 2 : 1) to avoid the formation of additional possible phases, for example, $Cs_3M^{III}{}_2Cl_9$ salts with a lower relative Cs content ($Cs:M^{III}$ = 1.5). As a result, the supernatants over the as-precipitated perovskites contain residual alkali metal salts, which can interfere with the following structural characterization of the products and need to be removed. Fig. 2 illustrates a typical workflow for the exemplary HTP preparation of CANBIC perovskite samples, including the steps of precursor transfer to the sample plate, precipitation of perovskites, purification of the as-deposited suspensions, as well as robot-assisted drop-casting of the purified samples to produce arrays of solid samples for spectral and structural characterization.

For each compositional domain, a bank of "focus" sample arrays can be produced using the same synthetic protocol along with the "master" plate to vary independently M^{III} and M^{I} sites and cover all possible compositions with different increments. In the case of CANBIC perovskites, several six 48-sample well-plates were produced of which two plates, the "master" plate with 0···100% Bi and a "focus" plate with 0···2% Bi were selected for detailed characterizations.

Selecting the array of HTP characterizations. Considering the possibility of the formation of multiple additional phases during the precipitation of double chloride elpasolites as well as possible deviations from the nominal (set at the synthesis) stoichiometry, the characterization of the structure and composition is essential for each and any of the produced samples. From the practical viewpoint, this requirement means that the speed of characterization should match the speed of the synthesis, thus requiring the development of an HTP characterization protocol that accompanies the robot-assisted HTP synthesis and combines structural and spectral components.

The structural characterization included the characterization of the phase, morphology, and composition of all samples by powder X-ray diffraction (XRD), scanning electron microscopy (SEM), and energy-dispersive X-ray spectroscopy (EDX). Though the characterization setups were not completely automatized and required a human operator, the measurements can be upscaled to a quasi-HTP regime. Specifically, XRD measurements were performed using an automated sample holder allowing the diffractometer to automatically measure a total load of 15 samples with a throughput of one 48-sample set per day (ESI,† Fig. S2). The quasi-HTP SEM and EDX measurements were performed on miniature sample arrays drop-casted on fragments of carbon tape fixed to a silicon wafer and allowing a 48-sample set to be loaded into the SEM chamber and measured during a single run.

The spectral characterizations included measurements of UV-Vis reflectance spectra, PL spectra, and PL excitation (PLE) spectra using both an automated plate-reader Tecan spectrometer and fast manual measurements with a miniature fiber-coupled UV-Vis spectrometer (StellarNet, USA), both modes requiring *ca.* 30 min per each of the spectral characterizations of a 48-sample plate.

The samples for structural and spectral measurements were produced on substrates of different geometry (plastic round well arrays for spectral measurements, detachable square 1 cm^2 glass substrates for XRD, carbon tape/silicon for SEM/EDX) by drop-casting either manually or using the Tecan pipetting robot. Fig. S2 in ESI† provides an overview of different types of samples (suspensions, drop-casted films) and measurement modes used in the present work.

In the following sections, we discuss a selected series of sample arrays with different binary and ternary M^{III} combinations, putting in each case a special focus on the non-additive properties that cannot be predicted as a linear combination of the properties of individual components and were found owing to the HTP screening. These include (i) compositional dependences of the PL properties of CANBIC perovskites, (ii) band-bowing effects observed for CANBSC perovskites, and (iii) compositional design of the bandgap of CANFBIC perovskites. Please refer to Table 1 for perovskite formulas and abbreviations.

2.2 Binary plates: the case of M^{III} = Bi + In

As we reported earlier, CANBIC perovskites show a strong dependence of PL quantum yield (PL QY) on the Bi fraction, showing PL QYs of up to 98% at 1–2 molar% Bi.[23,24] As these experiments were performed in a conventional manual regime, the range of Ag/Na ratio variations as well as steps of Bi/In ratio variation tested in these reports are limited. Here, we perform a more detailed HTP screening of the compositional dependences of PL properties of CANBIC perovskites producing the "master" plate (Bi 0···100%, Ag 0···100%) as well as a series of "focus" plates with different ranges of Bi and Ag fractions. A

Table 1 Full and short versions of brutto-formulas and abbreviations of the $Cs_2M^{I}M^{III}Cl_6$ compounds synthesized in the present work

M^{III} site	Full brutto-formula	Short brutto-formula	Abbreviation
Bi + In	$Cs_2Ag_xNa_{1-x}Bi_yIn_{1-y}Cl_6$	$Cs_2(Ag,Na)(Bi,In)Cl_6$	CANBIC
Bi + Sb	$Cs_2Ag_xNa_{1-x}Bi_ySb_{1-y}Cl_6$	$Cs_2(Ag,Na)(Bi,Sb)Cl_6$	CANBSC
In + Sb	$Cs_2Ag_xNa_{1-x}In_ySb_{1-y}Cl_6$	$Cs_2(Ag,Na)(In,Sb)Cl_6$	CANISC
In + Bi + Sb	$Cs_2(Ag,Na)In_x(Bi_ySb_{1-y})_{1-x}Cl_6$	$Cs_2(Ag,Na)(In,Bi,Sb)Cl_6$	CANIBSC
Fe + Bi + In	$Cs_2(Ag,Na)Fe_x(Bi_yIn_{1-y})_{1-x}Cl_6$	$Cs_2(Ag,Na)(Fe,Bi,In)Cl_6$	CANFBIC

 This journal is © The Royal Society of Chemistry 2024

Open Access Article. Published on 25 May 2024. Downloaded on 3/17/2026 1:04:52 PM.
This article is licensed under a Creative Commons Attribution 3.0 Unported Licence.

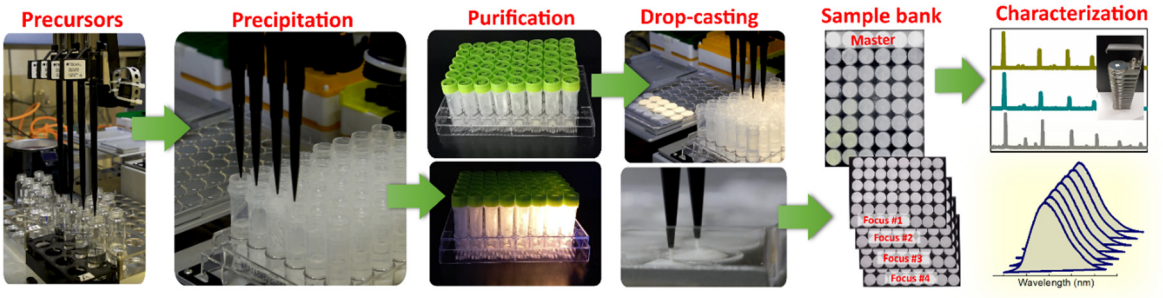

Fig. 2 Schematic workflow for HTP synthesis of CANBIC perovskites.

preliminary characterization showed that a combination of the "master" plate and the "focus" plate with 0···2% Bi provides the highest variation of PL properties, while the rest of the "focus" plates were found to be redundant. The "master" plate was subjected to the above-discussed comprehensive structural/spectral HTP characterization (see summary in Table S1, ESI†).

CANBIC – structure and phase. An XRD characterization showed almost all CANBIC samples to be single-phase products in the entire compositional domain of the "master" plate with all reflections in XRD patterns indexed as belonging to $Fm\bar{3}m$ cubic perovskite. Only In-pure samples with Ag/(Ag + Na) > 0.50 show the presence of small admixtures (most probably AgCl) along with the dominating CANBIC phase. Fig. 3(a) illustrates exemplary XRD patterns for two series of CANBIC perovskites with 50% Bi and 50% Ag, while the complete collection of "master" XRD patterns can be found in ESI† (Fig. S3).

Routinely, Rietveld refinement was performed for all collected XRD patterns allowing the phase purity to be evaluated and the lattice parameter of the cubic perovskite phase to be calculated. The "master" CANBIC plate showed a smooth monotonous dependence of the lattice parameter on the Bi and Ag fractions showing linear increase with increasing Bi fraction with no irregularities and extrema, indicating that CANBIC samples are single-phase solid solutions in the entire "master" compositional domain (see ESI,† Table S1 for numerical values of the lattice parameter).

CANBIC – morphology and composition. The CANBIC perovskites in the "master" plate are all microcrystalline powders formed by loosely aggregated polyhedra with a grain size of 1–5 μm (ESI,† Fig. S4). No specific correlations between the composition and grain size were found, with the crystal size showing a trend to increase for low Bi contents.

The case of CANBIC perovskites showed a reliable compositional control provided by the developed HTP synthesis. The actual Bi fractions were found to be very close to the nominal values (set at the synthesis in precursors) for all Ag/Na ratios tested in the "master" plate (ESI,† Table S1 and Fig. S5). Similarly, the actual Ag/Na ratio grows almost linearly with the nominal value showing no dependences on the Bi/In ratio. The Cl/M^{III} ratio was found to be between 5 and 6 for all "master" samples, with Ag-rich samples showing relatively larger Cl/M^{III} values closer to 6. The Cs/M^{III} rations were found to be within the range of 1.9–2.2, following the $Cs_2M^IM^{III}Cl_6$ stoichiometry expected for elpasolites.

CANBIC – spectral properties and PL QY. The CANBIC perovskites reveal broad-band PL in the visible spectral range centered at 550–650 nm depending on the composition and originating from the STE states.[23–25] The emission color varies from quasi-white to yellow to brown depending on the Bi and Ag contents (ESI,† Fig. S6). The In-pure samples containing both Ag and Na show no PL emission under the excitation at

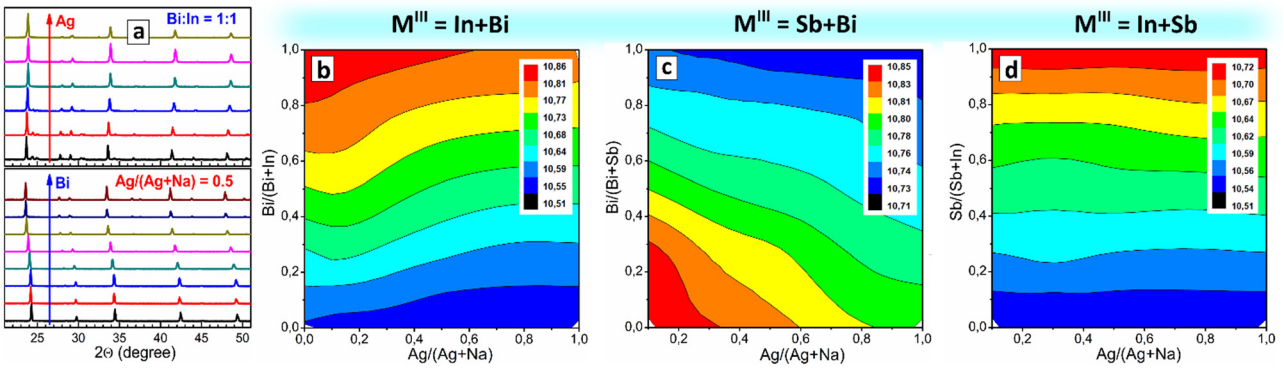

Fig. 3 (a) Exemplary XRD patterns of $Cs_2(Ag,Na)(Bi,In)Cl_6$ perovskites for samples with Ag/(Ag + Na) fraction varied from 0 to 1.00 at Bi/(Bi + In) = 0.50 (upper part) and with Bi/(Bi + In) fraction varied from 0 to 1.00 at Ag/(Ag + Na) = 0.50 (lower part); (b)–(d) lattice parameter of $Cs_2(Ag,Na)M^{III}Cl_6$ perovskites with M^{III} = In + Bi (b), M^{III} = Sb + Bi (c), and M^{III} = In + Sb (d) as a function of the M^{III} and M^I components. Maps in (b)–(d) are plotted by interpolating and smoothing data from 48 samples for each M^{III} combination. The evolution of the lattice parameter is presented by colors changing from blue to red with numerical values indicated as corresponding scales in (b)–(d).

Open Access Article. Published on 25 May 2024. Downloaded on 3/17/2026 1:04:52 PM.
This article is licensed under a Creative Commons Attribution 3.0 Unported Licence.

365 nm, but emit PL when excited at 254 nm, indicating larger bandgaps inaccessible for the 365-nm excitation, as shown in Table S1 (ESI†). At the same time, the Na-pure samples with no Ag show no PL emission under both excitations (ESI,† Fig. S6), indicating that lattice distortions from the presence of both Ag and Na are essential for the formation of the emissive STE states.

The absorption band edge of CANBIC perovskites shifts from *ca.* 380 nm to 450 nm as the Bi/In ratio is increased from 1–2% to 100%. Analysis of the absorption spectra showed a higher linearity of the absorption band edge plotted in the Tauc coordinates for allowed indirect transitions (ESI,† Fig. S7) as compared with a similar transformation using the Tauc coordinates for the direct transitions. The compositional variations of the indirect bandgap are smooth with no noticeable extrema and discontinuities (ESI,† Fig. S8 and Table S1).

The PL band maximum of CANBIC perovskites shows only a minor shift, from *ca.* 580 nm to *ca.* 640 nm, when the Bi fraction is increased by 4 orders of magnitude – from 0.01% to 100% (Fig. 4(a)). Variations of the Ag/Na ratio also exert only a limited effect on the spectral PL properties of CANBIC perovskites (ESI,† Table S1). When observed for the entire "master" plate, the PL maximum energy E_{PL} shows gradual changes without noticeable extrema, with the highest values (2.10–2.15 eV) observed for Bi-pure compounds regardless of Ag content, while the lowest E_{PL} values (below 1.9 eV) were found for Bi- and Na-rich perovskites (Fig. 4(b)).

In contrast to the variations of spectral PL properties, the compositional dependence of PL QY shows a rather sharp extremum observed in a relatively narrow range of Bi contents close to 1% but for a broad range of Ag/Na ratios, the PL QYs exceeding 90% in this compositional "summit" (Fig. 4(c)). We note that the position of the summit was identified by the HTP screening by the "master" and a "focus" plates of CANBIC samples, showing clear advantages of the developed HTP approach over the conventional point-wise trials.

2.3 Binary plates: the cases of M^{III} = Bi + Sb and In + Sb

The synthetic algorithm described in the previous section for CANBIC can be relatively easily extended to other M1 + M2 combinations, such as Bi + Sb and In + Sb with minimal adjustments, yielding $Cs_2Ag_xNa_{1-x}Bi_ySb_{1-y}Cl_6$ (CANBSC) and $Cs_2Ag_xNa_{1-x}In_ySb_{1-y}Cl_6$ (CANISC) perovskites, respectively. In this way, two 48-sample "master" CANBSC and CANSIC arrays were produced by the robot-assisted HTP setup using the same synthetic protocol and control script. A schematic of the combinatorial synthesis and the photographs of the final plates are presented in Fig. 1(b) and (c), respectively. A summary of the experimental data on the composition, structure, and spectral properties of CANBSC and CANSIC "master" plates is provided in ESI† (Tables S2 and S3, respectively).

2.3.1 CANBSC "master" plate. Recently we have reported on the open-atmosphere synthesis of Ag-pure CABSC perovskites with a Bi/In ratio varied from 0 to 1.00, showing a non-additive compositional dependence of their bandgap on the Bi fraction resulting in the band-bowing phenomenon.[26] Here, we extend the synthesis approach to the simultaneous variation of M^{III} and M^{I} components analogical to the above-discussed case of CANBIC perovskites.

CANBSC – structure and composition. An EDX study of the "master" CANBSC plate revealed Cs/M^{III} and Cl/M^{III} ratios to be close to 2 and 5–6, respectively, for almost all samples (ESI,† Table S2 and Fig. S9). These ratios are expected for the double $Cs_2M^{I}M^{III}Cl_6$ stoichiometry with a small chloride deficiency typically observed for the open-atmosphere RT synthesis protocols.[23,24,26] The deviations are, though, observed for Na-rich (90–100% Na) and Sb-rich (75–100% Sb) compositions, which show Cs/M^{III} = 1.7 and Cl/M^{III} close to 4.5, typical for double $Cs_3M^{III}{}_2Cl_9$ salts.

The XRD measurements corroborate the conclusions made from EDX data showing the Na- and Sb-rich samples to be indeed dominated by the double salt phases (ESI,† Fig. S10, samples A1–A4 and B1–B4). In all other cases, the cubic double perovskite phase is prevailing or solely present with the lattice parameter changing linearly with the change of x and y (Fig. 3(c)), indicating the formation of solid-solution perovskite products.

The actual Bi/(Bi + Sb) fraction derived from EDX closely matches the nominal values for all tested Ag/Na ratios (ESI,†

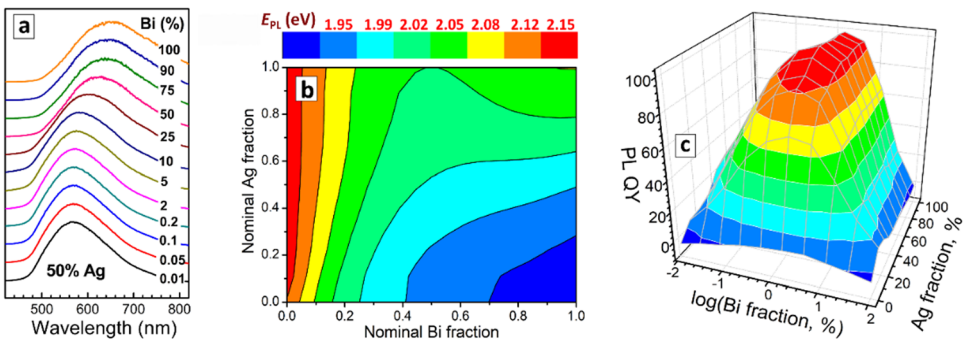

Fig. 4 (a) Exemplary normalized PL spectra of CANBIC perovskites with a nominal Ag fraction of 50% and varied Bi content y; (b) PL band maximum energy E_{PL} of CANBIC perovskites in the "master" plate as a function of nominal Bi and Ag fractions; (c) compositional dependence of PL QY of CANBIC perovskites built using PL spectra from "master" +"focus" plates (96 samples). The evolution of E_{PL} in (b) is presented by colors changing from blue to red with numerical values indicated in the corresponding scales on the figure top.

Open Access Article. Published on 25 May 2024. Downloaded on 3/17/2026 1:04:52 PM.
This article is licensed under a Creative Commons Attribution 3.0 Unported Licence.

Fig. S9) indicating a reliable control over the variable composition of the M^{III} component. At the same time, the actual Ag/(Ag + Na) fraction was found to deviate to higher values with respect to the nominal fraction for the Sb-enriched compositions with more than 50% Sb (ESI,† Fig. S9 and Table S2). Overall, despite the presence of an additional phase of double salts we still have a reliable control over the phase and composition of the CANBSC perovskites in the major part of the "master" compositional domain.

CANBSC – spectral properties. As we reported recently, the Ag-pure CABSC perovskites reveal a band-bowing effect showing lower indirect bandgaps for intermediate Bi/Sb ratios as compared to Bi-pure and Sb-pure compounds.[26] By inspecting the CANBSC "master" plate in the present work we found this phenomenon to be general for the samples with variable M^{I} compositions. As an example, Fig. 5(a) presents a set of absorption spectra of CANBSC perovskites with 80% Ag and a variable Sb content that shows the lowest bandgap of *ca.* 2.7 eV for the sample with 75% Sb, while the Bi- and Sb-pure samples reveal bandgaps of *ca.* 2.8 eV and 2.9 eV, respectively. At that, the variation of the Bi/Sb ratio does not result in any noticeable changes in the shape of the absorption band.

This band-bowing trend was found to be general for all tested Ag/Na variations resulting in the compositional dependence of the indirect bandgap demonstrated in Fig. 5(b). For all Ag/Na variations, the minimal bandgap was observed for Sb-enriched mixed compounds with 75–90% Sb (see also Table S2 in ESI†). At that, the increase in the Ag fraction at a constant y is accompanied by an ordinary and expected monotonous decrease of the bandgap with no special bowing effects.

The band-bowing effect can originate from multiple factors, including a local disorder induced by the random mixing of Bi^{3+} and Sb^{3+} cations having different radii,[55,56] as well as stem from electronic factors, in particular, from the non-equivalent contribution of Bi^{3+} and Sb^{3+} into the formation of the valence band maximum (VBM) and conduction band minimum (CBM).[57,58] Since for double perovskites, both M^{III} and M^{I} variation are expected to affect the orbital VBM/CBM composition,[57,58] the present results show a promising route to a fast screening of band-bowing-prone compositional domains to locate the global bandgap minimum.

We note that the density functional theory (DFT) calculations of the compositional bandgap dependence of CABSC perovskites typically show a monotonous bandgap evolution with varying Bi/Sb ratio[57–59] and the band-bowing effects observed experimentally can only be derived from DFT when spin–orbit coupling effects were taken into consideration.[59] Such calculations are very demanding on the computational power and have not been adapted to a high-throughput regime so far. In this situation, the present HTP screening methodology seems to be the best available solution to search for the band-bowing effects in the M^{III}-mixed double halide perovskites.

In contrast to CANBICs, CANBSC samples are mostly non-luminescent under the excitation at 365 nm with the PL emission observed only for the Bi-pure samples with non-zero silver contents and, as an exception, for a single mixed CANBSC sample with 10% Ag and 10% Sb (ESI,† Fig. S11).

2.3.2 CANISC "master" plate. Similar to the above case of M1 + M2 = Bi + Sb, the In + Sb pair can be introduced at variable ratios into the M^{III} position of double chloride perovskite using the same open-environment HTP synthesis protocol yielding the "master" arrays of $Cs_2Ag_xNa_{1-x}In_ySb_{1-y}Cl_6$ samples that cover the entire range of x and y variations.

The outcomes of EDX/XRD characterization of the CANSIC plate are similar to those collected for the CANBSC perovskite array. In particular, the Na, Sb-rich samples with $x < 0.10$ and $y < 0.25$ show the Cs/M^{III} and Cl/M^{III} ratios close to 1.5 and 4.5, respectively, indicating the predominant formation of double $Cs_3M^{III}{}_2Cl_9$ salts (ESI,† Table S3 and Fig. S12). This conclusion is supported by XRD showing the presence of double salts in this compositional domain (ESI,† Fig. S13, samples A1–A3 and B1, B2). The rest of the samples show typical cubic perovskite symmetry with the lattice parameter changing linearly with the compositional variations (Fig. 3(d)), indicative of the formation of the single-phase solid solutions. The actual In/Sb and Ag/Na ratios are very close to the nominal ones showing a reliable control over the M^{I} and M^{III} components (ESI,† Fig. S12).

In contrast to CABSC perovskites, the CANISC array does not show any indications for the band-bowing effects in absorption spectra demonstrating a gradual decrease of the indirect bandgap with growing antimony content (ESI,† Fig. S8).

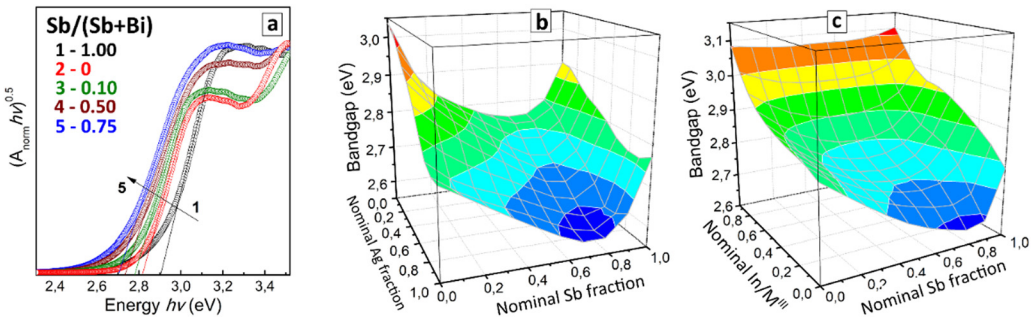

Fig. 5 (a) Exemplary absorption spectra of $Cs_2(Ag,Na)(Bi,Sb)Cl_6$ perovskites 80% Ag and varied Sb content, presented in the coordinates of the Tauc equation for indirect allowed interband transitions. (b) and (c) Compositional dependences of the indirect bandgaps of CANBSC (b) and CANIBSC (c) perovskites.

Open Access Article. Published on 25 May 2024. Downloaded on 3/17/2026 1:04:52 PM.
This article is licensed under a Creative Commons Attribution 3.0 Unported Licence.

The CANISC samples were found to be mostly non-luminescent under the excitation at 365 nm with a single exception of relatively bright PL emission for a sample with 100% Na and 10% Sb (ESI,† Fig. S11). The appearance of a single emissive sample, which was reproduced for several consecutive HTP syntheses, provides an additional argument in favor of the proposed HTP screening approach that can be very instrumental in revealing non-additive properties of double perovskites with mixed M^{I} and M^{III} sites, especially those showing in a relatively narrow range of compositions.

2.4 Ternary plates: the case of M^{III} = In + Bi + Sb

The almost ideal mutual miscibility of three pairs of cations, Bi + In, Bi + Sb, and In + Sb, on the M^{III} site of double chloride perovskites served as an inspiration for further increase of the complexity of the elpasolite systems scrutinized by the current HTP screening.

To realize ternary In + Bi + Sb mixing on the M^{III} site we fixed the nominal silver content at 70% and instead varied In content along the shorter axis of the Eppendorf plate as discussed above in the introductory part. Such HTP synthesis yielded a "master" plate of $Cs_2(Ag,Na)In_x(Bi_ySb_{1-y})_{1-x}Cl_6$ (CANIBSC) perovskites (Fig. 1(c)) with Bi/Sb ratio changing from 0 to 1.00 along the larger plate axis and In/M^{III} fraction varied from 0 to 0.95 along the smaller plate axis. A summary of the characterizations of the CANIBSC sample array is presented in ESI† (Table S4).

CANIBSC – composition and structure. An XRD study of CANIBSC perovskites showed them as single-phase cubic perovskites in the entire tested compositional domain with no appreciable admixtures of other phases (ESI,† Fig. S14). The lattice parameter of CANIBSC perovskites was calculated using Rietveld refinement of the XRD patterns and evolves linearly with the variations of the Bi/Sb and In/M^{III} ratios (Fig. 6(a)), indicating the formation of single-phase solid solutions.

An EDX inspection showed the Cs/M^{III}, Cl/M^{III} (ESI,† Table S4), and M^{I}/M^{III} (ESI,† Fig. S15, left panel) ratios to be close to 2.0, 5.5–6.0, and 1.0 in all cases indicating the double perovskite $Cs_2M^{I}M^{III}Cl_6$ stoichiometry of the final products.

The actual fractions of In/M^{III} and Bi/(Bi + Sb) derived from EDX data (Fig. 7(a) and (b)) are close to the nominal values showing a reliable control over the composition of the ternary M^{III} component. The Ag fraction was found to be generally close to the nominally set value of 70% with positive deviations up to 0.8–0.9 observed for In- and Bi-poor compositions (Fig. 7(c) and ESI,† Table S4). SEM inspection of the CANIBSC perovskites (data available but not shown) revealed them to be microcrystalline powders with no noticeable trends in the morphology observed for different compositions.

Summarizing the structural characterization of the CANIBSC plate we note that the present results show the feasibility of the synthesis of double chloride perovskites with three different metals on the M^{III} site and a mixed M^{I} site while maintaining reasonably confident control over the stoichiometry and phase composition.

In total, six different metals – Cs, Ag, Na, In, Bi, and Sb, are introduced simultaneously and at different proportions into single-phase cubic perovskites produced within the same HTP synthesis protocol. As such, the present system illustrates the potential of the proposed HTP screening approach allowing the complexity of the composition to be relatively easily elevated to seven constituents with further variations possible, such as the design of more complex M^{I} sites and/or anion-exchange-driven transformations like those reported by us for CABSC perovskites.[26] These variations are expected to yield new high-entropy materials with non-additive properties which can hardly be predicted from the properties of individual components and require the HTP screening approach to be found and evaluated.

In contrast to the expectations based on general experience, the high-entropy alloying was found to yield materials with increased stability as compared to individual components, resulting from overcoming the mixing enthalpy barriers.[60,61] A combination of strong lattice disorder with a high short-range ordering allows new functional properties to be expected from the high-entropy materials, including piezoelectric, thermoelectric, photoelectric, and other effects, uncharacteristic for similar materials of lower complexity. Typically, studies of high-entropy materials are focused on metal alloys combining five or more components, but the focus gradually shifts to metal compounds, including halide perovskites.[60,61]

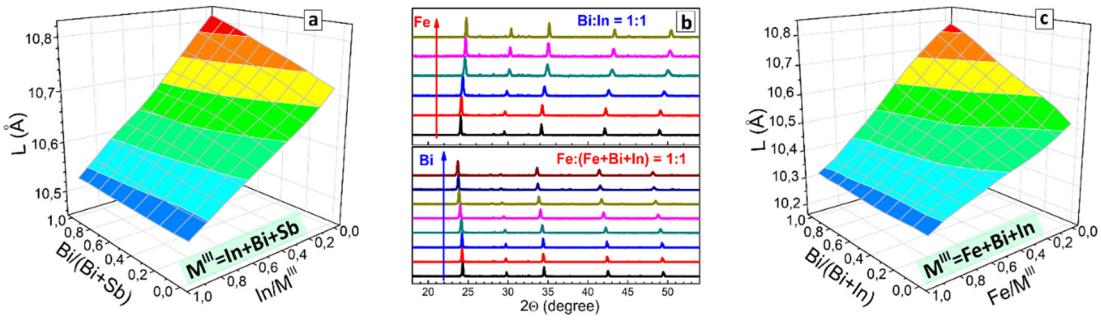

Fig. 6 (a), (c) Lattice parameter of $Cs_2(Ag,Na)M^{III}Cl_6$ perovskites with M^{III} = In + Bi + Sb (a) and Fe + Bi + In (c) as a function of the fractions of different M^{III} components. Maps in (a), (c) are plotted by interpolating and smoothing data from 48 "master" samples for each M^{III} combination. (b) Exemplary XRD patterns of $Cs_2(Ag,Na)(Fe,Bi,In)Cl_6$ perovskites for samples with Fe/M^{III} fraction varied from 0 to 0.95 at Bi/(Bi + In) = 0.50 (upper part) and with Bi/(Bi + In) fraction varied from 0 to 1.00 at Fe/M^{III} = 0.50 (lower part).

Open Access Article. Published on 25 May 2024. Downloaded on 3/17/2026 1:04:52 PM.
This article is licensed under a Creative Commons Attribution 3.0 Unported Licence.

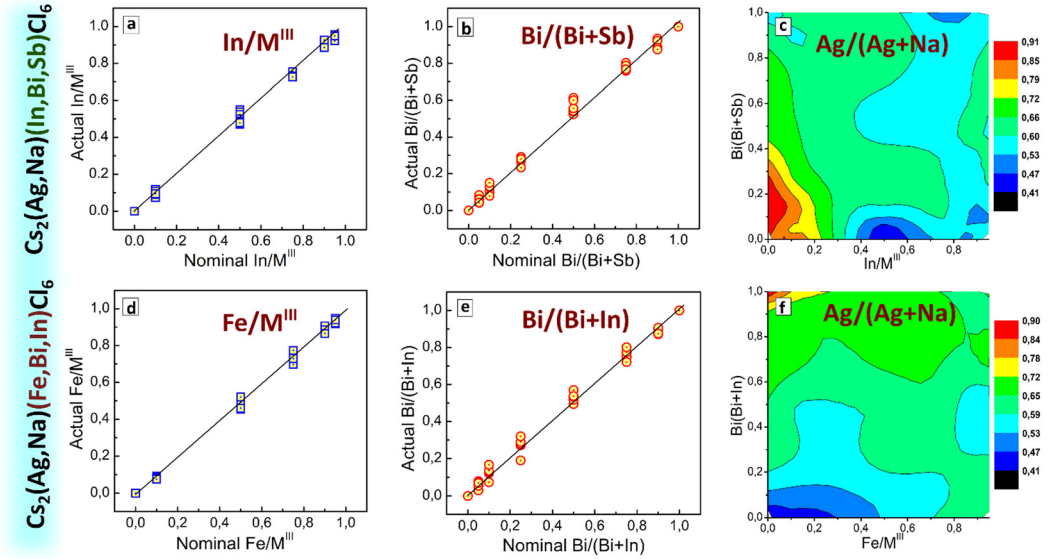

Fig. 7 Summary of EDX data on $Cs_2(Ag,Na)(In,Bi,Sb)Cl_6$ perovskites (a)–(c) and $Cs_2(Ag,Na)(Fe,Bi,In)Cl_6$ perovskites (d)–(f): actual *versus* nominal ratios of M^{III} components (a), (b), (d), (e) and 2D maps showing actual Ag/(Ag + Na) ratios as functions of nominal fractions of M^{III} components (c), (f). The evolution of the Ag/Na fraction in (c), (f) is presented by colors changing from blue to red with numerical values indicated in the corresponding scales.

To evaluate the complexity state reached in the present report we calculated the configurational entropy ΔS_{conf} as a measure of the disordering degree along the approach developed for high-entropy metal alloys as $\Delta S_{conf} = -R\sum_{i=1}^{N} x_i \ln x_i$,[61] where R is the universal gas constant (8.314 J (mol K)$^{-1}$), N is the number of metal elements in the perovskite, and x_i is the molar fraction of metal i. As generally accepted, the materials with $\Delta S_{conf} \geq 1.5R$ are referred to as high-entropy materials, while the compounds with $1.0R \leq \Delta S_{conf} \leq 1.5R$ and $\Delta S_{conf} \leq 1.0R$ are considered medium-entropy and low-entropy materials, respectively.[61]

The CANIBSC perovskites showed ΔS_{conf} values between 1.2 and 1.3 (ESI,† Table S4) categorizing them as medium-entropy materials. Therefore, further elevation of complexity is required to enter the domain of high-entropy materials, which can be realized in the frame of the proposed HTP screening by extending the combinatorial synthesis to other combinations of M^I, M^{III} as well as to alloying on A^I and X sites, currently occupied by Cs and Cl.

CANIBSC – spectral properties. Analogous to CANBIC and CANBSC perovskites, the CANIBSC family shows continuous absorption bands with no distinct maxima, which can be linearized in the Tauc coordinates for allowed indirect transitions with linear band edge sections large enough for reliable bandgap calculations (see summary in ESI,† Table S4).

All CANIBSC perovskites were found to show the band-bowing behavior typical for CANBSC compounds, which gradually becomes less distinct as the Indium fraction is elevated from 0 to 95% (Fig. 5(c)). At that, the range of Bi/Sb ratios corresponding to minimal bandgaps remains roughly unchanged with the In variations and similar to that of binary CANBSC perovskites (Fig. 5(b)). In this sense, Indium acts as a modifier of the band-bowing behavior of Bi/Sb perovskites, not disrupting the band-bowing trend but increasing generally the absolute values of bandgaps as Indium content is increased.

When excited at 365 nm, the CANIBSC perovskites were found to be mostly non-luminescent with the exceptions of Bi-pure compounds and a small "island" of Sb-poor compounds (ESI,† Fig. S11).

2.5 Ternary plates: the case of M^{III} = Fe + Bi + In

Recently we have reported a series of double $Cs_2(Ag,Na)(Fe,In)Cl_6$ (CANFIC) perovskites produced using an open-atmosphere RT approach similar to that applied earlier to CANBIC and CABSC perovskites.[54] Indium was found to act as a "catalyst" that induced the formation of cubic CANFIC perovskites even when present at very small amounts, 0.5–1.0%, while no single-phase products could be produced in the absence of In^{3+}. In the present work, we further develop this approach showing that a similar structure-dictating effect can also be observed for Bi^{3+} additions.

Structure-directing role of Bi^{3+}. The precipitation of $Cs_2(Ag,Na)FeCl_6$ with 100% Fe on the M^{III} site results in the formation of a partially amorphous multi-phase product (ESI,† Fig. S16a).

The situation changes dramatically in the presence of even small amounts of Bi^{3+}. The precipitation with 5 mol% Bi^{3+} yields highly crystalline products with polygonal grains (ESI,† Fig. S16b) showing a well-defined XRD pattern of a cubic double perovskite with no other phases detectable. The actual Cs/M^{III}, Cl/M^{III}, and Ag/(Ag + Na) fractions identified by EDX (data available but not shown) are close to 2.0, 6.0, and 0.5, following the expected stoichiometry.

Similar to the case of In^{3+},[54] a further increase in the Bi content from 5% to 100% results in a series of cubic perovskite solid solutions with a correspondingly evolving lattice parameter

Open Access Article. Published on 25 May 2024. Downloaded on 3/17/2026 1:04:52 PM. This article is licensed under a Creative Commons Attribution 3.0 Unported Licence.

(ESI,† Fig. S16c) and absorption band edge shifting to lower wavelengths as the fraction of Bi is increased (ESI,† Fig. S16d).

"Master" and "focus" Fe + Bi + In plate – structure and composition. Profiting from the capability of both In^{3+} and Bi^{3+} to stimulate independently the formation of single-phase cubic iron-based double perovskites we developed a synthetic approach allowing all three metals, Fe, Bi, and In, to be combined on the M^{III} site while still retaining the single-phase solid-solution perovskite structure of the products. This approach is very similar to that used for the synthesis of the above-discussed In + Bi + Sb ternary samples, only with a considerably larger concentration of HCl requiring the synthesis to be performed in a closed-ventilated environment (see ESI† for more details of the synthesis).

The "master" array of $Cs_2Ag(Na)Fe_x(Bi_yIn_{1-y})_{1-x}Cl_6$ (CANFBIC) was synthesized by varying the Bi/In ratio from 0 to 1.00 along the longer axis of the Eppendorf plate while increasing the Fe/(Fe + Bi + In) fraction from 0 to 0.95 along the shorter axis. A summary of the structural and spectral properties of the "master" set is provided in ESI† (Table S5). Considering the strong effect that small amounts of both Indium and Bismuth exert on the structure of the final iron-based products, another "focus" array of samples was prepared to target the specific Fe/M^{III} range of 95.0–99.5%.

In both cases, the samples for structural and spectral characterization were produced by drop-casting from 2-propanol, suspensions followed by solvent evaporation under ambient conditions. At that, the relative humidity (RH) of the environment during the solvent evaporation was found to considerably impact the stability of the "focus" samples while having no notable influence on the stability of the "master" sample plate. In particular, the "focus" samples kept for the evaporation at RH = 60% showed clear signs of the decomposition of some of the iron-rich samples visible by characteristic color changes, which were considerably less pronounced when the evaporation was performed at RH = 15% (ESI,† Fig. S17). For this reason, we adopted RH = 15% for the preparation of all samples of the iron-based perovskites. After complete solvent evaporation, both "master" and "focus" samples retain prolonged stability (months) regardless of the environmental humidity when kept at RH under 70%.

An XRD inspection of the "master" plate showed all the CANFBIC samples to be single-phase cubic perovskites (see exemplary powder XRD profiles in Fig. 6b as well as the whole set of diffractograms in Fig. S18, ESI†). Only some of the samples with the intermediate Iron content (D6–D8 in Fig. S18, ESI†) showed a lower crystallinity and small phase admixtures, the reason for which is not clear at the moment.

The lattice parameter of the CANFBIC perovskites calculated by Rietveld refinement of the powder XRD patterns showed a linear variation with both the Bi/In ratio and relative Iron content (Fig. 6(c)) indicating that the products were single-phase solid solutions.

An XRD inspection of the "focus" CANFBIC plate indicated most of the samples to be cubic double perovskites but also revealed an "instability island" for the Iron- and Bismuth-rich samples (ESI,† Fig. S19, samples D6–D8, E6–E8, and F7, F8). These samples show color signs of decomposition closely matched by the corresponding XRD patterns showing the presence of a mixture of phases instead of the cubic perovskite motif typical for the rest of the CANFBIC samples (marked by a blue contour in Fig. S19, ESI†). Again, the origins of the instability of the samples in this compositional domain, which is reproducible in many syntheses, are unclear and require a dedicated study.

An SEM study of the "master" CANFBIC set (ESI,† Fig. S20) showed all the products to be loosely aggregated microcrystals that reveal a clear trend for the increase of the grain size with increasing iron content. The "master" samples with the maximal iron content (95%) contain crystals with a size above 10 μm, some of the grains growing as large as 30–40 μm with well-defined polygonal shapes.

An EDX survey of the "master" sample array showed a very close correspondence between nominal Fe/M^{III} and Bi/(Bi + In) fractions and actual fractions found in the corresponding samples (Fig. 7(d) and (e)), attesting to a precise control over the composition of the M^{III} component of the CANFBIC perovskites. The actual Ag/(Ag + Na) ratio was found to be close to 50% for most of the samples, showing higher values only for Fe-poor samples (at Fe/M^{III} $\leq$ 0.10, see Fig. 7(f) and Table S5 in ESI†). The ratios of Cs/M^{III}, Cl/M^{III}, and M^{I}/M^{III} are generally close to 2.0, 6.0, and 1.0, respectively for all tested samples (ESI,† Fig. S15, right panel, and Table S5) showing that the CANFBIC perovskites have the desired stoichiometry of double perovskites.

"Master" and "focus" Fe + Bi + In plate – spectral properties. Analogous to the recently reported binary CANFIC perovskites, the ternary CANFBIC compounds show continuous absorption spectra with the edge spanning over the entire visible range depending on their compositions. The absorption edge can be linearized in the Tauc coordinates for allowed indirect electron transitions allowing the indirect bandgap to be evaluated from the absorption spectra (see E_g summary in Fig. 8(a) and ESI,† Table S5).

The variation of the Fe/M^{III} ratio exerts the most decisive effect on the position of the absorption band edge as exemplified in Fig. 7(b) for a fixed Bi/(Bi + In) fraction of 50%. The absorption edge shifts from *ca.* 420 nm for CANBIC to *ca.* 620 nm for CANFBIC with 95% Iron, while variations of Bi/In ratio have only a marginal effect on the absorption band position at such high Iron content (Fig. 8(c)). As the bandgap shift is dominated by the variations of Fe/M^{III} the compositional E_g "map" shows a monotonous decrease from the Fe- and Bi-poor samples to Fe- and Bi-rich samples (Fig. 8(a)), with the minimal bandgap in the "master" plate being 1.91 eV (x = 1.00, y = 0.95, Table S5 in ESI†).

A further shift of the bandgap to lower values was achieved in the "focus" CANFBIC sample array with the iron content varied between 95.0% and 99.5%. The compositional "map" of indirect bandgaps (Fig. 8(d)), as well as bandgap dependences on the Bi/In ratio plotted for specific iron contents in Fig. 8(e), show a band-bowing behavior, with the bandgaps of Bi/In-mixed compounds being lower than the bandgaps of Bi-pure or In-pure perovskites. In the case of 99.5% Fe, the band-

 This journal is © The Royal Society of Chemistry 2024

Open Access Article. Published on 25 May 2024. Downloaded on 3/17/2026 1:04:52 PM.
This article is licensed under a Creative Commons Attribution 3.0 Unported Licence.

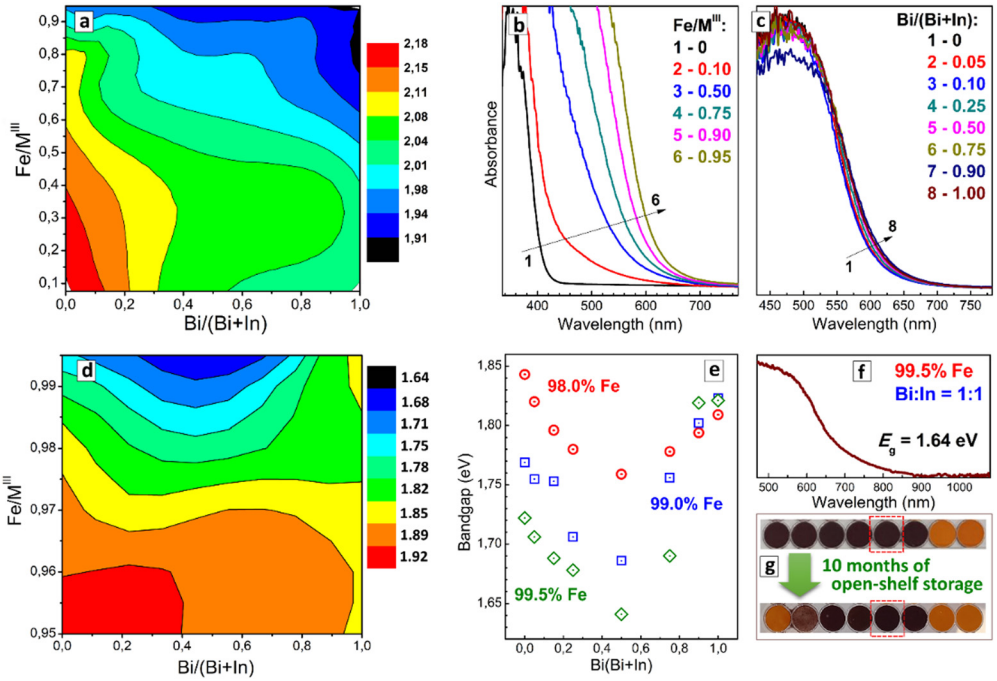

Fig. 8 (a), (d) and (e) Bandgap of $Cs_2(Ag,Na)(Fe,Bi,In)Cl_6$ perovskites in the "master" (a) and "focus" (d), (e) plates as a function of the perovskite composition. The evolution of the Fe/M^{III} ratio in (a), (d) is presented by colors changing from blue to red with numerical values indicated in the corresponding scales. (b), (c) Absorption spectra of CANFBIC perovskites produced at different Fe/M^{III} ratios with constant Bi/(Bi + In) fraction of 0.50 (b) and at different Bi/(Bi + In) ratios with constant Fe/M^{III} fraction of 0.95 (c). (f) The absorption spectrum of the "champion" CANFBIC perovskite with the lowest bandgap. (g) Photographs of a section of the "focus" CANFBIC plate corresponding to Fe/M^{III} = 99.5% and Bi/(B + In) varied from 0 to 1.00 directly after the perovskite synthesis and after 10 months of open-shelf storage (ambient conditions, RH *ca.* 50%, in the dark). The "champion" sample is marked with a dashed rectangle. M^{III} = Fe + Bi + In.

bowing effect can be attributed to the above-discussed instability of the samples observed by visual inspection and XRD. However, the band-bowing behavior is also observed for stable single-phase samples with lower iron contents, down to 97.0–97.5% (Fig. 8(d)). This observation indicates that the band-bowing effect is inherent for this compositional domain of CANFBIC perovskites similar to the above-discussed binary Bi + Sb and ternary In + Bi + Sb perovskites.

A"champion" CANFBIC sample, in terms of the lowest bandgap, was found for 99.5% Fe and a Bi/(Bi + In) fraction of 0.50. This sample showed an indirect bandgap of 1.64 eV, corresponding to an absorption edge at *ca.* 700 nm tailing down to 900 nm (Fig. 8(f)). This is the lowest bandgap observed for chloride double perovskites in our experiments so far, and it falls into the range typical for lead-based perovskite PV absorbers, such as methylammonium lead iodide (1.56 eV) or bromide (2.30 eV).[2,5] At the same time, this value is observed for a chloride compound, indicating a strong decrease in the energy of ligand-to-metal electron transition in CANFBIC perovskites as compared to $FeCl_3$, probably, due to a large delocalization of the charge carriers in such perovskites. Currently, we pursue the aim of producing optically transparent CANFBIC films that could be used to test the PV activity of these compounds.

It should also be noted that the single-phase CANFBIC samples show high stability toward ambient humidity. This stability is illustrated by no changes observed in the color and the absorption spectrum (Fig. 8(g)) as well as in XRD patterns (data not shown) of the "champion" CANBIFC compound with 99.5% Fe and Bi/(Bi + In) = 0.50 after a long storage (about 10 months) in open ambient conditions.

3 Conclusions

A high-throughput screening of lead-free double chloride perovskites $Cs_2M^IM^{III}Cl_6$ is presented, combining open-environment combinatorial robot-assisted synthesis with high-throughput structural and spectral characterizations. The screening yielded *ca.* 350 elpasolite compounds combining Ag^+ and Na^+ on the M^I site and featuring two (Bi + In, Bi + Sb, and In + Sb) or three (In + Bi + Sb and Fe + Bi + In) metal cations on the M^{III} site.

The automated approach allows various M^{III} combinations to be screened using generally the same synthesis routine, scheme of precursor preparation, and robotized platform with minimal adjustments required to adapt for new M^{III} combinations. By equalizing the reactivity of different M^{III} species in precursors, arrays of double perovskite samples with M^{III} = Bi + In (CANBIC), M^{III} = Bi + Sb (CANBSC), and M^{III} = In + Sb (CANISC) were produced including 48 single-phase microcrystalline samples per array with the fractions of M^I and M^{III} components independently varied from 0 to 100%. This procedure was further

Open Access Article. Published on 25 May 2024. Downloaded on 3/17/2026 1:04:52 PM.
This article is licensed under a Creative Commons Attribution 3.0 Unported Licence.

expanded to ternary cation combinations on M^{III} sites with a fixed nominal Ag/Na ratio. In this way, two 48-sample arrays of cubic double perovskites were produced with M^{III} = In + Bi + Sb (CANIBSC) and M^{III} = Fe + Bi + In (CANFBIC) with all samples showing a single-phase solid-solution character with reliably controlled ratios of the M^{III} components. We note that the combination of three metal cations on the M^{III} sites of double halide perovskites has not been reported so far.

The automated synthesis routine is flexible allowing the range of M^{I} and M^{III} variations to be varied by adjusting the component ratios and concentrations in the precursors while using the same automated routine to focus on specific compositional domains with a higher resolution. This approach was applied for the CANBIC system to focus on the most luminescent samples with Bi content ranging between 0 and 2% as well as for the CANFBIC system to vary the iron content between 95.0% and 99.5%.

The structural characterization of the produced families of samples revealed reliable compositional control over the stoichiometry of the products, very similar morphology for the samples within the arrays as well as monotonous changes of the lattice parameters indicating the formation of solid-solution compounds in the entire range of possible compositions. At the same time, the spectral characterization revealed a series of non-additive properties, including a ''volcano''-shape of the dependence of PL QY of CANBIC perovskites on Bi/In and Ag/Na ratios as well as a band-bowing behavior of the bandgap for CANBSC perovskites with Bi and Sb alloyed at the M^{III} sites.

For the CANBIC family, the HTP screening revealed a broad ''high-efficiency-PL island'' where PL QY exceeds 90%, at Bi fractions of 0.2–2.0 mol% and silver fractions ranging from 20 to 80 mol%.

In the case of the CANBSC family, the band-bowing effects were found to peak at Sb/(Bi + Sb) ratios of 0.75–0.90 for all tested Ag/Na ratios. The more complex CANIBSC perovskites combining In, Bi, and Sb on the M^{III} site were found to inherit the band-bowing behavior from the parental CANBSC family showing similar compositional E_g dependences, the minimal values observed at Sb/(Bi + Sb) of *ca.* 0.75.

By profiting from a structure-directing effect of In^{3+} and Bi^{3+} cations that drive the Cs–Ag–Na–Fe–Bi(In)–Cl system to the exclusive formation of single-phase cubic double perovskites, a new family of elpasolites was produced combining Fe, Bi, and In on the M^{III} site while retaining single-phase character for a broad range of iron content spanning from 0 to 95%. Such Fe-based chloride elpasolites combining three metals on the M^{III} site have not been reported before.

A domain of Fe-richer compositions was also assessed by producing the CANFBIC family with iron content ranging from 95.0 to 99.5%. A large ''stability island'' was found in this range extending as far as 99.5% of Fe and 75% Bi in the Bi + In component with unprecedentedly low bandgaps. The indirect bandgap of 1.64 eV was found for a CANFBIC sample with 99.5% iron and Bi/(Bi + In) ratio of 0.50, which is probably the lowest bandgap value reported so far for a chloride double perovskite.

Evaluations of the configurational entropy of CANIBSC and CANFBIC perovskites with ternary M^{III} sites showed them to fall into the category of medium-entropy alloys, outlining the perspectives of the automated screening to reach the domain of high-entropy compounds by further increasing the compositional complexity of other crystallographic positions.

The HTP screening approach reported here is universal and can be further extended to new combinations on M^{I} and M^{III} sites with minimal technical modifications. Adaptation of the anion-exchange procedures, similar to those reported by us for CABSC perovskites,[26] to the regime of automated synthesis is expected to expand the applicability of the present HTP procedures and allow lower-bandgap bromide and iodide perovskite as well as perovskite-inspired derivatives of chloride elpasolites to be subjected to the automated screening to discover non-additive properties and target new materials promising for PV applications.

Author contributions

O. Stroyuk: conceptualization (lead), investigation (equal), writing – original draft preparation (lead); O. Raievska: investigation (lead), methodology (lead); M. Daum: investigation (equal), writing – review & editing (equal); J. Hauch: conceptualization (equal), project administration (lead), writing – review & editing (equal); C. J. Brabec: conceptualization (equal), funding acquisition (lead), writing – review & editing (equal).

Conflicts of interest

There are no conflicts to declare.

Acknowledgements

The authors gratefully acknowledge the financial support of The German Federal Ministry for Economic Affairs and Climate Action (project Pero4PV, FKZ: 03EE1092A) and The Bavarian State Government (project ''ELF-PV-Design and development of solution-processed functional materials for the next generations of PV technologies'', no. 44-6521a/20/4).

Notes and references

1 R. Wang, T. Huang, J. Xue, J. Tong, K. Zhu and Y. Yang, *Nat. Photonics*, 2021, **15**, 411.
2 J. Y. Kim, J. W. Lee, H. S. Jung, H. Shinand and N. G. Park, *Chem. Rev.*, 2020, **120**, 7867.
3 Z. Guo, A. K. Jena, G. M. Kim and T. Miyasak, *Energy Environ. Sci.*, 2022, **15**, 3171.
4 A. Fakharuddin, M. K. Gangishetty, M. Abdi-Jalebi, S. H. Chin, A. R. bin Mohd Yusoff, D. N. Congreve, W. Tress, F. Deschler, M. Vasilopoulou and H. J. Bolink, *Nat. Electronics*, 2022, **5**, 203.
5 F. Ma, Y. Zhao, Z. Qu and J. You, *Acc. Mater. Res*, 2023, **4**, 716.

 This journal is © The Royal Society of Chemistry 2024

Open Access Article. Published on 25 May 2024. Downloaded on 3/17/2026 1:04:52 PM.
This article is licensed under a Creative Commons Attribution 3.0 Unported Licence.

6 I. López-Fernández, D. Valli, C. Y. Wang, S. Samanta, T. Okamoto, Y. T. Huang, K. Sun, Y. Liu, V. S. Chirvony, A. Patra, J. Zito, L. De Trizio, D. Gaur, H. T. Sun, Z. Xia, X. Li, H. Zeng, I. Mora-Seró, N. Pradhan, J. P. Martínez-Pastor, P. Müller-Buschbaum, V. Biju, T. Debnath, M. Saliba, E. Debroye, R. L. Z. Hoye, I. Infante, L. Manna and L. Polavarapu, *Adv. Funct. Mater.*, 2024, **34**, 2307896.
7 Y. Gao, Y. Pan, F. Zhou, G. Niu and C. Yan, *J. Mater. Chem. A*, 2021, **9**, 11931.
8 X. Li, X. Gao, X. Zhang, X. Shen, M. Lu, J. Wu, Z. Shi, V. L. Colvin, J. Hu, X. Bai, W. W. Yu and Y. Zhang, *Adv. Sci.*, 2021, **8**, 2003334.
9 L. A. Muscarella and E. M. Hutter, *ACS Energy Lett.*, 2022, **7**, 2128.
10 O. Stroyuk, O. Raievska, J. Hauch and C. J. Brabec, *Angew. Chem., Int. Ed.*, 2023, **62**, e202212668.
11 W. Ning and F. Gao, *Adv. Mater.*, 2019, **31**, 1900326.
12 A. Dubey, S. L. Sanchez, J. Yang and M. Ahmadi, *Chem. Mater.*, 2024, **36**, 2165.
13 S. Ahmed, M. A. Gondal, A. S. Alzahrani, M. Parvaz, A. Ahmed and S. Hussain, *ACS Appl. Energy Mater.*, 2024, **7**, 1382.
14 W. Yu, Y. Zou, H. Wang, S. Qi, C. Wu, X. Guo, Y. Liu, Z. Chen, B. Qu and L. Xiao, *Chem. Soc. Rev.*, 2024, **53**, 1769.
15 X. He, Y. Deng, D. Ouyang, N. Zhang, J. Wang, A. A. Murthy, I. Spanopoulos, S. M. Islam, Q. Tu, G. Xing, Y. Li, V. P. Dravid and T. Zhai, *Chem. Rev.*, 2023, **123**, 1207.
16 Y. Peng, T. N. Huq, J. Mei, L. Portilla, R. A. Jagt, L. G. Occhipinti, J. L. MacManus-Driscoll, R. L. Z. Hoye and V. Pecunia, *Adv. Energy Mater.*, 2021, **11**, 2002761.
17 H. Tang, Y. Xu, X. Hu, Q. Hu, T. Chen, W. Jiang, L. Wang and W. Jiang, *Adv. Sci.*, 2021, **8**, 2004118.
18 S. Jiang, M. Liu, D. Zhao, Y. Guo, J. Fu, Y. Lei, Y. Zhang and Z. Zheng, *Phys. Chem. Chem. Phys.*, 2024, **26**, 4794.
19 J. Luo, X. Wang, S. Li, J. Liu, Y. Guo, G. Niu, L. Yao, Y. Fu, L. Gao, Q. Dong, C. Zhao, M. Leng, F. Ma, W. Liang, L. Wang, S. Jin, J. Han, L. Zhang, J. Etheridge, J. Wang, Y. Yan, E. H. Sargent and J. Tang, *Nature*, 2018, **563**, 541.
20 D. Zhu, J. Zito, V. Pinchetti, Z. Dang, A. Olivati, L. Pasquale, A. Tang, M. L. Zaffalon, F. Meinardi, I. Infante, L. De Trizio, L. Manna and S. Brovelli, *ACS Energy Lett.*, 2020, **5**, 1840.
21 C. Y. Wang, P. Liang, R. J. Xie, Y. Yao, P. Liu, Y. Yang, J. Hu, L. Shao, X. W. Sun, F. Kang and G. Wei, *Chem. Mater.*, 2020, **32**, 7814.
22 Q. Hu, G. Niu, Z. Zheng, S. Li, Y. Zhang, H. Song, T. Zhai and J. Tang, *Small*, 2019, **15**, 1903496.
23 O. Stroyuk, O. Raievska, A. Barabash, M. Batentschuk, A. Osvet, S. Fiedler, U. Resch-Genger, J. Hauch and C. J. Brabec, *J. Mater. Chem. C*, 2022, **10**, 9938.
24 O. Stroyuk, O. Raievska, A. Barabash, C. Kupfer, A. Osvet, V. Dzhagan, D. R. T. Zahn, J. Hauch and C. J. Brabec, *Mater. Adv.*, 2022, **3**, 7894.
25 O. Stroyuk, O. Raievska, D. R. T. Zahn and C. J. Brabec, *The Chem. Rec.*, 2024, **24**, e202300241.
26 O. Stroyuk, O. Raievska, A. Barabash, R. W. Hooper, V. K. Michaelis, J. Hauch and C. J. Brabec, *J. Mater. Chem. C*, 2024, **12**, 533.
27 Z. Li, M. A. Najeeb, L. Alves, A. Z. Sherman, V. Shekar, P. C. Parrilla, I. M. Pendleton, W. Wang, P. W. Nega, M. Zeller, J. Schrier, A. J. Norquist and E. M. Chan, *Chem. Mater.*, 2020, **32**, 5650.
28 S. Chen, Y. Hou, H. Chen, X. Tang, S. Langner, N. Li, T. Stubhan, I. Levchuk, E. Gu, A. Osvet and C. J. Brabec, *Adv. Energy Mater.*, 2018, **8**, 1701543.
29 N. Meftahi, M. A. Surmiak, S. O. Fürer, K. J. Rietwyk, J. Lu, S. Ruiz Raga, C. Evans, M. Michalska, H. Deng, D. P. McMeekin, T. Alan, D. Vak, A. S. R. Chesman, A. J. Christofferson, D. A. Winkler, U. Bach and S. P. Russo, *Adv. Energy Mater.*, 2023, **13**, 2203859.
30 R. K. Gunasekaran, J. Jung, S. W. Yang, J. Yun, Y. Yun, D. Vidyasagar, W. C. Choi, C. L. Lee, J. H. Noh, D. H. Kim and S. Lee, *InfoMat*, 2023, **5**, e12393.
31 S. Chen, L. Zhang, Y. Liu, Z. Zhang, Y. Li, W. Cai, H. Lv, Y. Qin, Q. Liao, B. Zhou, T. Yan, J. Ren, S. Chen, X. Xiang, S. Dai, S. K. So, X. Wang, S. Yang and B. Xu, *J. Mater. Chem. A*, 2021, **9**, 25502.
32 Y. An, C. A. Riccardo Perini, J. Hidalgo, A. F. Castro-Mendez, J. N. Vagott, R. Li, W. A. Saidi, S. Wang, X. Li and J. P. Correa-Baena, *Energy Environ. Sci.*, 2021, **14**, 6638.
33 S. Moradi, S. Kundu, M. Awais, Y. Haruta, H. D. Nguyen, D. Zhang, F. Tan and M. I. Saidaminov, *Small*, 2023, **19**, 2301037.
34 J. G. Manion, A. H. Proppe, G. E. J. Hicks, E. H. Sargent and D. S. Seferos, *ACS Appl. Mater. Interfaces*, 2020, **12**, 26026.
35 K. Higgins, M. Ziatdinov, S. V. Kalinin and M. Ahmadi, *J. Am. Chem. Soc.*, 2021, **143**, 19945.
36 S. Chen, L. Zhang, L. Yan, X. Xiang, X. Zhao, S. Yang and B. Xu, *Adv. Funct. Mater*, 2019, **29**, 19055487.
37 S. Moradi, S. Kundu, M. Rezazadeh, V. Yeddu, O. Voznyy and M. I. Saidaminov, *Commun. Mater.*, 2022, **3**, 13.
38 M. A. Surmiak, T. Zhang, J. Lu, K. J. Rietwyk, S. Ruiz Raga, D. P. McMeekin and U. Bach, *Sol. RRL*, 2020, **4**, 2000097.
39 A. Wieczorek, A. G. Kuba, J. Sommerhäuser, L. N. Caceres, C. M. Wolff and S. Siol, *J. Mater. Chem. A*, 2024, **12**, 7025.
40 Y. Zhao, J. Zhang, Z. Xu, S. Sun, S. Langner, N. T. Putri Hartono, T. Heumueller, Y. Hou, J. Elia, N. Li, G. J. Matt, X. Du, W. Meng, A. Osvet, K. Zhang, T. Stubhan, Y. Feng, J. Hauch, E. H. Sargent, T. Buonassisi and C. J. Brabec, *Nat. Commun.*, 2021, **12**, 2191.
41 S. Sun, N. T. P. Hartono, Z. D. Ren, F. Oviedo, A. M. Buscemi, M. Layurova, D. X. Chen, T. Ogunfunmi, J. Thapa, S. Ramasamy, C. Settens, B. L. DeCost, A. G. Kusne, Z. Liu, S. I. P. Tian, I. M. Peters, J. P. Correa-Baena and T. Buonassisi, *Joule*, 2019, **3**, 1437.
42 X. Cai, Y. Zhang, Z. Shi, Y. Chen, Y. Xia, A. Yu, Y. Xu, F. Xie, H. Shao, H. Zhu, D. Fu, Y. Zhan and H. Zhang, *Adv. Sci.*, 2022, **9**, 2103648.
43 J. Yang and A. Mannodi-Kanakkithodi, *MRS Bull.*, 2022, **47**, 940.
44 J. C. Stanley, F. Mayr and A. Gagliardi, *Adv. Theory Simul.*, 2020, **3**, 1900178.
45 W. Hu, L. Zhang and Z. Pan, *ACS Appl. Mater. Interfaces*, 2022, **14**, 21596.
46 A. Jain, O. Voznyy and E. H. Sargent, *J. Phys. Chem. C*, 2017, **121**, 7183.

Open Access Article. Published on 25 May 2024. Downloaded on 3/17/2026 1:04:52 PM.
This article is licensed under a Creative Commons Attribution 3.0 Unported Licence.

47 S. Lu, Q. Zhou, Y. Ouyang, Y. Guo, Q. Li and J. Wang, *Nat. Commun.*, 2018, **9**, 3405.
48 X. Diao, Y. Diao, Y. Tang, G. Zhao, Q. Gu, Y. Xie, Y. Shi, P. Zhu and L. Zhang, *Sci. Rep.*, 2022, **12**, 12633.
49 J. Gebhardt, A. Gassmann, W. Wei, A. Weidenkaff and C. Elsässer, *Mater. Des.*, 2023, **234**, 112324.
50 Z. Li, Q. Xu, Q. Sun, Z. Hou and W. J. Yin, *Adv. Funct. Mater.*, 2019, **29**, 1807280.
51 Y. Cai, W. Xie, Y. T. Teng, P. C. Harikesh, B. Ghosh, P. Huck, K. A. Persson, N. Mathews, S. G. Mhaisalkar, M. Sherburne and M. Asta, *Chem. Mater.*, 2019, **31**, 5392.
52 J. G. Park, S. W. Park and K. H. Hong, *Nanotechnology*, 2022, **33**, 485706.
53 J. Yang, P. Manganaris and A. Mannodi-Kanakkithodi, *Digital Discovery*, 2023, **2**, 856.
54 O. Stroyuk, O. Raievska, A. Barabash, J. Hauch and C. J. Brabec, *J. Mater. Chem. C*, 2023, **11**, 6867.
55 J. Im, C. C. Stoumpos, H. Jin, A. J. Freeman and M. G. Kanatzidis, *J. Phys. Chem. Lett.*, 2015, **6**, 3503.
56 G. E. Eperon, T. Leijtens, K. A. Bush, R. Prasanna, T. Green, J. T. W. Wang, D. P. McMeekin, G. Volonakis, R. L. Milot, R. May, A. Palmstrom, D. J. Slotcavage, R. A. Belisle, J. B. Patel, E. S. Parrott, R. J. Sutton, W. Ma, F. Moghadam, B. Conings, A. Babayigit, H. G. Boyen, S. Bent, F. Giustino, L. M. Herz, M. B. Johnston, M. D. McGehee and H. J. Snaith, *Science*, 2016, **354**, 861.
57 A. Goyal, S. McKechnie, D. Pashov, W. Tumas, M. Van Schilfgaarde and V. Stevanovic, *Chem. Mater.*, 2018, **30**, 3920.
58 Z. Li, S. R. Kavanagh, M. Napari, R. G. Palgrave, M. Abdi-Jalebi, Z. Andaji-Garmaroudi, D. W. Davies, M. Laitinen, J. Julin, M. A. Isaacs, R. H. Friend, D. O. Scanlon, A. Walsh and R. L. Z. Hoye, *J. Mater. Chem. A*, 2020, **8**, 21780.
59 H. Chen, S. Ming, M. Li, B. Wang and J. Su, *J. Phys. Chem. C*, 2021, **125**, 11271.
60 X. Wang, J. Yang, X. Wang, M. Faizan, H. Zou, K. Zhou, B. Xing, Y. Fu and L. Zhang, *J. Phys. Chem. Lett.*, 2022, **13**, 5017.
61 Y. Wang, J. Liu, Y. Song, J. Yu, Y. Tian, M. J. Robson, J. Wang, Z. Zhang, X. Lin, G. Zhou, Z. Wang, L. Shen, H. Zhao, S. Grasso and F. Ciucci, *Small Methods*, 2023, **7**, 2201138.

 This journal is © The Royal Society of Chemistry 2024